# Grid-Current Control of a Differential Boost Inverter With Hidden *LCL* Filters

Songwei Huang, Fen Tang, Zhen Xin, Qi Xiao, and Poh Chiang Loh

***Abstract*—Single-phase differential boost inverter, built from two identical dc–dc boost converters, has been suggested as an alternative to the usual connection of a dc–dc boost converter to a standard full-bridge inverter. Some control schemes for controlling it have also been proposed, but mostly for voltage regulation, supplying a standalone load, rather than grid-current control. Moreover, it has never been identified that two *LCL* filters are hidden in the differential boost topology. Problems related to their associated resonances have therefore not been discussed, especially their variations with duty ratios. It is thus necessary here to unmask the hidden *LCL* filters, which upon clarification, permits vast knowledge from grid-current control of a standard *LCL*-filtered inverter to be extended for differential inverter control. However, the extension involves many challenges introduced by the varying resonance frequencies, nonlinearity, and many control options permitted by the differential boost inverter. These challenges are addressed now with simulation and experimental results provided for verifying direct grid-current regulation of a differential boost inverter.**

***Index Terms*—Active resistive damping, differential boost inverter, grid-current control, power decoupling, resonance.**

## I. Introduction

RENEWABLE energy sources, such as photovoltaic modules and fuel cells, usually generate low dc terminal voltages, which are subsequently interfaced to the ac grid using dc–ac boost inverters [1], [2]. In turn, the boost inverters are mostly built by connecting classical dc–dc boost converters to dc–ac full-bridge inverters [3], [4]. The former can be referred to as the front stage, whereas the latter forms the rear stage of a two-stage configuration. Both stages usually have their own control schemes, which nonetheless will still affect each other unintentionally, unless a large electrolytic capacitor for maintaining a fairly constant dc-link voltage is inserted between the two stages. This electrolytic capacitor has however a short lifespan, and in a single-phase system, it must constantly tolerate second-order oscillating power flowing through it. Hence, it may hence be a major concern, in addition to the switch of the front dc–dc boost converter, which must usually tolerate the high input current alone.

Manuscript received October 10, 2017; revised December 28, 2017 and February 17, 2018; accepted March 13, 2018. Date of publication March 20, 2018; date of current version November 19, 2018. This work was supported by the Fundamental Research Funds for the Central Universities under Grant 2017YJS175. Recommended for publication by Associate Editor X. Ruan. *(Corresponding author: Fen Tang.)*

S Huang, Q. Xiao, and P. C. Loh are with the National Active Distribution Network Technology Research Center, Beijing Jiaotong University, Beijing 100044, China (e-mail:

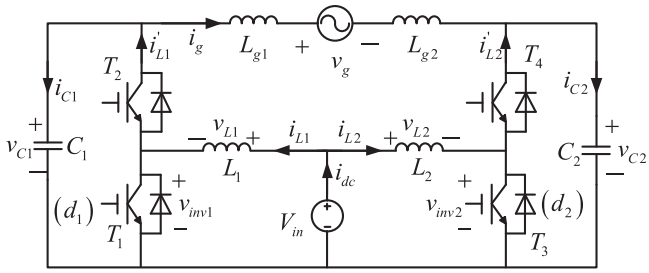


Fig. 1. Grid-connected differential boost dc–ac inverter.

Alternatively, differential boost inverters, such as shown in Fig. 1, can be considered, which for single-phase connection involve two identical bidirectional dc–dc boost converters [5]. The number of switches demanded by the single-phase differential inverter is thus reduced to four, which undoubtedly is the same as in a standard full-bridge inverter. These switches must however be higher voltage-rated, since output voltages produced by the two boost converters must be higher than their common input voltage, while yet generate an ac voltage that is almost equal to the grid voltage. It is thus a tradeoff, in exchange for minimizing the two earlier concerns associated with the two-stage topology. First, a single switch tolerating the full input current no longer exists, since input current of the differential boost inverter has been channeled to two dc–dc boost converters. Second, a large electrolytic capacitor is no longer necessary, since the two output capacitor voltages of the differential boost inverter are no longer constant, but vary with the grid or other frequencies, which it must generate.

Moreover, with its symmetrical structure, the differential boost inverter in Fig. 1 can divert second-order oscillating power to its two capacitors $C_1$ and $C_2$, which then permits constant current to be supplied by its input dc source. This capability has been referred to as power decoupling in the literature, which in terms of control, can be realized with waveform shaping [6]–[8], rule-based control [9], and/or various current-feedback schemes [10], [11]. For all schemes (and all power decoupling topologies), the second-order oscillating power has merely been

directed to existing or added reactive components for storage, since its elimination is generally not possible for a single-phase system. Related losses thus exist. Despite that, power decoupling may still be necessary, especially when the input source is sensitive to large current ripple. Its realization, together with other control features, may however be complicated by nonlinearity of the differential boost inverter, when compared with a standard full-bridge inverter with only voltage-buck capability [4], [5], [12].

Control developments for the differential boost inverter are thus not as rapid, but like the standard full-bridge inverter, they target either standalone or grid-connected mode. So far, the former has received more attention with the differential inverter regulated as a voltage source for supplying linear and/or nonlinear loads. An example can be found in [5], where a sliding-mode controller has been proposed for dynamic improvement. However, the scheme has not included power decoupling, which may not be easily realized with sliding-mode control. A classical double-loop control scheme with an inner inductor-current and an outer capacitor-voltage loop has hence been proposed in [13], which permits power decoupling to be incorporated. The scheme is however still voltage regulated, which renders it unsuitable for grid-connected operations.

Instead, the one-cycle controller developed in [14] may be considered for grid operation, if accuracy can be compromised slightly, since grid current is indirectly controlled through other variables. Another possibility is the current-control together with voltage-control double mode (CC-VC) method documented in [15], where one boost converter in Fig. 1 is current regulated, whereas the other is voltage regulated. The two boost converters are thus no longer symmetrical, which may compromise power decoupling with more harmonics expected at the ac and dc sides of the differential boost inverter. The latter may gradually lead to a reduction of lifetime of the input dc source [16].

While presenting its control method, Lu *et al.* [11] has also mentioned resonance experienced by the differential boost inverter, while supplying its standalone load. However, without a grid inductance, issues related to resonance are not as complex, and with a sizable resistive component in the standalone load, resonance damping is already "built-in," and hence not an issue. In [15], a fixed *LC* resonance, associated with the differential inverter when it is tied to the grid, has also been identified. However, it will be shown hereon that this resonance is oversimplified, because passive components at the dc side of the differential inverter have been ignored. The simplification has hence led to the less accurate conclusion of a single fixed resonance, which more correctly, should be two resonances, whose frequencies vary with the inverter duty ratios.

These resonances will be proven in Section II, after identifying the two hidden *LCL* filters in the grid-connected differential boost inverter. Identification of the hidden filters then permits grid-current regulation of the differential boost inverter to be extended from vast knowledge already established for a standard *LCL*-filtered full-bridge inverter. The extension, however, involves many fundamental thoughts, brought by nonlinearity and many control options available to the differential boost inverter. These issues will now be progressively addressed in Section III, before a direct grid-current control scheme is proposed in the same section. Auxiliary functions such as power decoupling and active damping will then be introduced in Section IV for further enhancing the grid and input current qualities, before verifying overall performances in Section V using results from simulations and experiments. Experimental results for the CC-VC scheme in [15] will also be presented in Section V for comparison with the proposed scheme, before findings are concluded in Section VI.

## II. Grid Connection Through Hidden *LCL* Filters

A description of the grid-connected differential boost inverter in Fig. 1 is presented first with the purpose of defining passive components and variables marked in the figure. Hidden *LCL* filters formed by the passive components are then modeled, from which concerns related to varying resonances are clarified.

### A. Configuration

The differential boost inverter in Fig. 1 is assembled with two identical dc–dc boost converters. Input current $i_{\rm dc}$ from the dc source $V_{\rm in}$ will therefore split into two currents $i_{L1}$ and $i_{L2}$, flowing through the two DC inductors $L_1$ and $L_2$ ($L_1 = L_2 = L$). Likewise, two output voltages $v_{C1}$ and $v_{C2}$ will be sustained across the two output capacitors $C_1$ and $C_2$ ($C_1 = C_2 = C$), and for symmetry, the grid inductance has been halved into $L_{g1}$ and $L_{g2}$ ($L_{g1} = L_{g2} = L_o/2$). These grid inductances are in series with the grid voltage $v_g$, and are hence carrying the same grid current $i_g$. Additionally, the grid voltage $v_g$ can be expressed as

$$v_g + L_o \frac{di_g}{dt} = v_{C1} - v_{C2} \tag{1}$$

where the differential capacitor voltage $(v_{C1} - v_{C2})$ must ideally be sinusoidal, if both $v_g$ and $i_g$ are sinusoidal.

The differential capacitor voltage can hence be denoted as

$$v_o = v_{C1} - v_{C2} = V_o \sin(\omega_0 t + \theta) \tag{2}$$

where $V_o$, $\omega_0$, and $\theta$ represent its amplitude, angular frequency, and phase measured with reference to the grid voltage $v_g = V_g \sin(\omega_0 t)$. Half of this differential voltage can then be added to a common dc bias $V_{\rm dc}$, whereas the other half subtracted from the same bias to form the following two capacitor voltages:

$$\begin{cases} v_{C1} = V_{\rm dc} + \dfrac{v_g}{2} + \dfrac{L_o}{2}\dfrac{di_g}{dt} \\ v_{C2} = V_{\rm dc} - \dfrac{v_g}{2} - \dfrac{L_o}{2}\dfrac{di_g}{dt} \end{cases}. \tag{3}$$

Voltage $V_{\rm dc}$ is therefore a common voltage component, which must be set such that the minimums of $v_{C1}$ and $v_{C2}$ are always greater than the dc input voltage $V_{\rm in}$, in order for both dc–dc boost converters to function properly [10]. Upon ensuring that, each capacitor voltage can then be expressed as

$$v_{Cj} = \frac{V_{\rm in} - v_{Lj}}{1 - d_j} \tag{4}$$

where $j = 1$ or 2 represents the left or right dc–dc boost converter in Fig. 1, $v_{Lj}$ denotes the voltage across each dc inductance $L_j$, and $d_j$ denotes the duty ratio of the lower switch of each boost converter. It should further be noted that the analysis is based on average model, which means all variables have been assumed constant during the switching period $T_s$. Moreover, at instances where $L_j$ is small, (4) may be approximated as

$$v_{Cj} \approx \frac{V_{\text{in}}}{1 - d_j}. \tag{5}$$

Returning to (3), a unique implication deduced is most parameters of the differential boost inverter in Fig. 1 can be split into their differential-mode (DM) and common-mode (CM) components. The former can be expressed as $x_{\text{DM}} = (x_1 - x_2)/2$, where $x_{\text{DM}}$ can be voltage $v_{\text{DM}}$, current $i_{\text{DM}}$ or duty cycle $d_{\text{DM}}$ of $v_{Cj}$, $i_{Lj}$ or $d_j$, respectively. The latter can be expressed as $x_{\text{CM}} = (x_1 + x_2)/2$ for representing CM components of the same parameters. According to [11], small-signal modeling can then be applied separately to the DM and CM components for deriving approximate transfer functions for the nonlinear differential boost inverter. The procedure begins with defining a quiescent operating point, whose parameters are notated as $V_{C1} = V_{C2} = V_C$, $I_{L1} = I_{L2} = I_L$ and $D_1 = D_2 = D$. According to [11], the transfer function for relating the DM capacitor voltage to the DM duty cycle and transfer function for relating the CM dc inductor current to the CM duty cycle can then be derived as (6) and (7), respectively

$$G_{d2v\_\text{GC}}(s) = \frac{\hat{v}_{\text{DM}}(s)}{\hat{d}_{\text{DM}}(s)} = \frac{-LL_oI_Ls + V_CL_o(1-D)}{LCL_os^2 + \left[L_o(1-D)^2 + 2L\right]} \tag{6}$$

$$G_{d2i\_\text{PD}}(s) = \frac{\hat{i}_{\text{CM}}(s)}{\hat{d}_{\text{CM}}(s)} = \frac{CV_Cs + (1-D)I_L}{LCs^2 + (1-D)^2}. \tag{7}$$

These transfer functions will subsequently be used for analyzing stability of the differential boost inverter in a later section [11].

### *B. Hidden LCL Filters*

Mostly, resonances experienced by an inverter are assumed to be caused by passive components at either its ac or dc side only. This may be true for a standard full-bridge inverter with a large dc-link electrolytic capacitor. It is however not appropriate for an inverter with a smaller film capacitor, including the differential boost inverter in Fig. 1. In other words, all passive components must be considered when analyzing resonances, even though they are in different ac and dc frequency frames. Their respective influences can, in fact, be projected by reflecting the dc inductors $L_1$ and $L_2$ to the ac frame, which conceptually is similar to transformers.

Expressions for the reflected inductors $L_1'$ and $L_2'$ can then be derived from the following differential equation at the dc side of the inverter:

$$v_{\text{inv}j} = V_{\text{in}} - \frac{L_j di_{Lj}}{dt}. \tag{8}$$

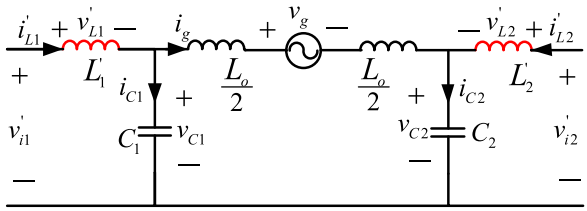


Fig. 2. Equivalent circuit in ac frame with two hidden *LCL* filters.

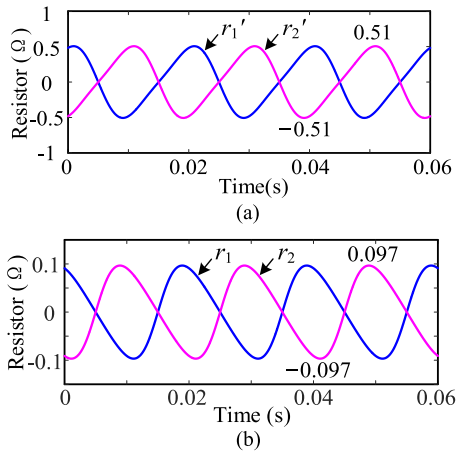


Fig. 3. Waveforms of (a) $r_j'$ and (b) $r_j$.

Further noting that voltage and current conversion functionalities of the inverter can be expressed as

$$i'_{Lj} = i_{Lj}(1 - d_j) \tag{9}$$

$$v_{Cj} = \frac{v_{\text{inv}j}}{1 - d_j} \tag{10}$$

where a prime$'$ symbol has been added to parameters reflected from the dc to ac frame. Substituting them into (8) then leads to

$$v_{Cj} = \frac{V_{\text{in}}}{1 - d_j} - \frac{L_j}{(1-d_j)^2}\frac{di'_{Lj}}{dt} - \frac{L_j}{(1-d_j)^3}\frac{d(d_j)}{dt}i'_{Lj}. \tag{11}$$

In terms of a circuit, the right side of (11) can be interpreted as a reflected source $v'_{ij} = \frac{V_{\text{in}}}{(1-d_j)}$, a reflected inductor $L'_j = \frac{L_j}{(1-d_j)^2}$, and a reflected resistor $r'_j = \frac{L_j}{(1-d_j)^3}\frac{d(d_j)}{dt}$ in series, and they are all dependent on duty ratio $d_j$. Together, they then parallel with capacitor $C_j$, since they share the same voltage. The reflected equivalent circuit in the ac frame of the differential boost inverter can thus be drawn as shown in Fig. 2, from which two features should be explained. The first involves the unmasking of two hidden *LCL* filters of the differential boost inverter, formed by ($L_1'$, $C_1$, and $L_o/2$) and ($L_2'$, $C_2$, and $L_o/2$), respectively. Both filters therefore include reflected inductors, implying their resonances will vary with duty ratio $d_j$.

The second involves reflected resistors $r_1'$ and $r_2'$, whose resistances vary according to Fig. 3(a), plotted using parameters provided in Table I. Both resistances are thus symmetrical about an average of zero, meaning they can unconventionally become negative, even though not simultaneously. Their

TABLE I
CIRCUIT AND CONTROL PARAMETERS OF A DIFFERENTIAL BOOST INVERTER

| Parameter | Value | Parameter | Value |
|---|---|---|---|
| Circuit parameters | | | |
| $L_1, L_2$ | 860 $\mu$H | $C_1, C_2$ | 47 $\mu$F |
| $L_o$ | 500 $\mu$H | $V_{\text{in}}$ | 100 or 70 V |
| $V_{\text{dc}}$ | 230 V | $V_g$ | $110\sqrt{2}$ V |
| $I_g$ | $2.122\sqrt{2}$ A | $f_s$ | 10 kHz |
| $f_0$ | 50 Hz | | |
| Single-loop grid-current control parameters | | | |
| $K_p$ | 12 | $K_r$ | 2300 |
| Power decoupling control parameters | | | |
| $K_{p,\text{PD}}$ | 4 | $K_{r,PD,100\text{ Hz}}$ | 800 |
| $K_{r,\text{PD}}$, 200 Hz | 100 | $K_{r,PD,300\text{ Hz}}$ | 10 |
| Active damping control parameters | | | |
| $R_1, R_2$ | 1 $\Omega$ | | |

"negative" presences must hence be nullified by respective positive virtual resistances inserted in series. These virtual resistances additionally help to damp resonances, which will be discussed in the Section III. In the meantime, both $r_1'$ and $r_2'$ are not included in Fig. 2, since they will not noticeably change the resonance frequencies, but their omission will greatly simplify transfer function derived for $i_{C1}/v_{i1}'$ in (12) shown at the bottom of this page. From (12), resonance frequencies of its four poles can then be derived as (13) and (14)

$$\omega_{reH}^2 = \frac{1}{2CL}\left(\frac{1}{m_1^2}+\frac{1}{(A-m_1)^2}+2x + \sqrt{\left(\frac{1}{m_1^2}-\frac{1}{(A-m_1)^2}\right)^2+4x^2}\right) \tag{13}$$

$$\omega_{reL}^2 = \frac{1}{2CL}\left(\frac{1}{m_1^2}+\frac{1}{(A-m_1)^2}+2x - \sqrt{\left(\frac{1}{m_1^2}-\frac{1}{(A-m_1)^2}\right)^2+4x^2}\right) \tag{14}$$

where $m_j = 1/(1-d_j)$, $A = m_1 + m_2 = 2V_{\text{dc}}/V_{\text{in}}$, and $x = L/L_o$.

The determined resonance frequencies are therefore dependent on duty ratio $d_j$, capacitor bias voltage $V_{\text{dc}}$ in (3), and input voltage $V_{\text{in}}$, in addition to the usual passive component values. Assuming now that $V_{\text{dc}}$ and $V_{\text{in}}$ are fixed, $d(\omega_{reH}^2)/dm_1$ versus $m_1$ and $x$ can be plotted in Fig. 4(a) for showing that the square of the higher resonance frequency $\omega_{reH}^2$ reaches its minimum at $m_1 = V_{\text{dc}}/V_{\text{in}}$ for all values of $x$. As for the lower resonance frequency $\omega_{reL}$, the same observation of its square being minimum at $m_1 = V_{\text{dc}}/V_{\text{in}}$ can be concluded from Fig. 4(b), as long as $x$ is larger than 0.5. This condition has been ensured by

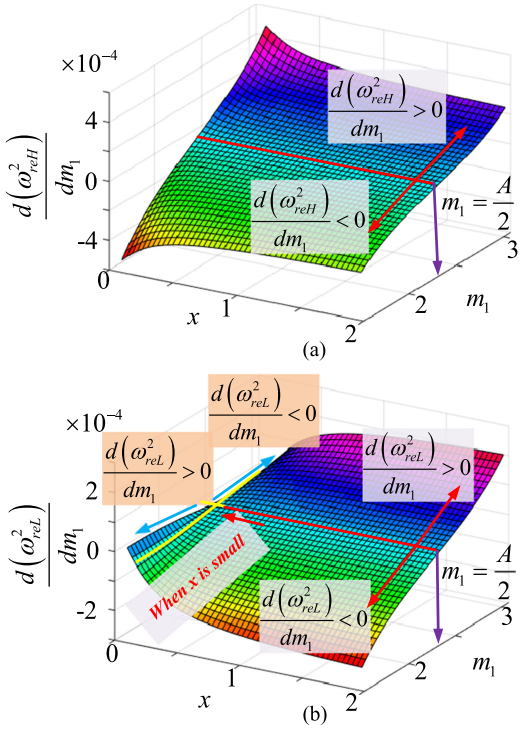


Fig. 4. Plots of (a) $d(\omega_{reH}^2)/dm_1$ versus $m_1$ and $x$ (b) $d(\omega_{reL}^2)/dm_1$ versus $m_1$ and $x$.

parameters chosen in Table I, implying that minimums of both resonances can be analyzed at the same $m_1 = V_{\text{dc}}/V_{\text{in}}$, which as understood from (3) and (5), corresponds to instants when the ac capacitor voltage components are zero. Confirmation of these observations can be deduced from Bode diagram plotted in Fig. 5 using (12) and parameters in Table I, but with different values of the duty ratio (or $m_j = 1/(1-d_j)$). Findings from the diagram can then be summarized, as follows.

1) Two resonances exist, whose frequencies $\omega_{reL}$ and $\omega_{reH}$ are not fixed, but vary with the inverter duty ratio $d_j$.
2) Maximums of $\omega_{reL}$ and $\omega_{reH}$ occur when $d_j$ is at its maximum and minimum values.
3) Minimums of $\omega_{reL}$ and $\omega_{reH}$ occur when $m_1 = 1/(1-d_1) = V_{\text{dc}}/V_{\text{in}}$, at which ac components of the capacitor voltages are zero.

The ranges of variation in Fig. 5 are, in fact, between 344 and 404 Hz for $\omega_{reL}$, and between 1510 and 1530 Hz for $\omega_{reH}$. It should however be noted that these ranges are applicable only when the dc input voltage $V_{\text{in}}$ is 100 V. Upon lowering $V_{\text{in}}$ to 70 V, the new ranges read from Fig. 6 are between 241 and 285 Hz for $\omega_{reL}$, and between 1488 and 1496 Hz for $\omega_{reH}$. These changes are expected, since according to (13) and (14), $V_{\text{in}}$ is inversely proportional to $A$, which in turn, appears only in the denominators of $\omega_{reL}$ and $\omega_{reH}$. It is therefore important to consider the lowest resonance frequency caused by the

$$\frac{i_{C1}}{v_{i1}'} = \frac{Cs\left(L_o + Lm_2^2 + CLL_o m_2^2 s^2\right)}{L_o + Lm_1^2 + Lm_2^2 + CLL_o m_1^2 s^2 + CLL_o m_2^2 s^2 + 2CL^2 m_1^2 m_2^2 s^2 + C^2 L^2 L_o m_1^2 m_2^2 s^4} \tag{12}$$

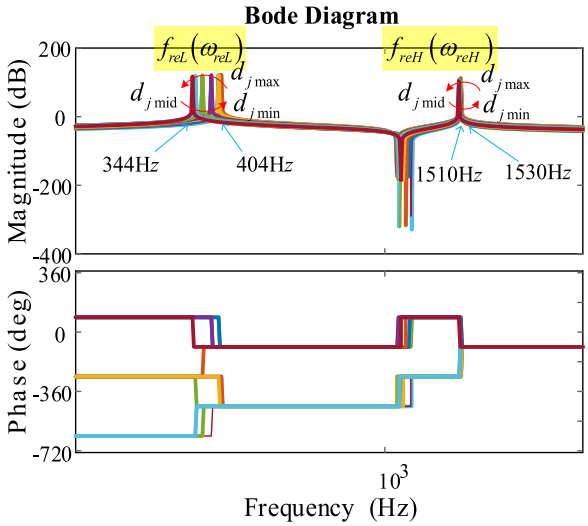


Fig. 5. Bode diagram of $i_{C1}/v'_{i1}$ with input voltage at 100 V.

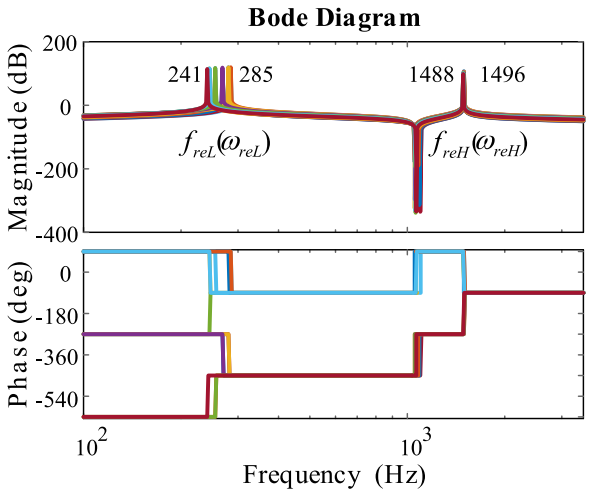


Fig. 6. Bode diagram of $i_{C1}/v'_{i1}$ with input voltage at 70 V.

smallest anticipated input voltage when designing the control and damping schemes later.

## III. Grid-Current Control

Upon identifying the hidden *LCL* filters, grid-current regulation of a differential boost inverter can be extended from the more mature grid-current regulation of a standard *LCL*-filtered full-bridge inverter. The extension is however not straightforward, because of nonlinearity and more control choices available to the differential boost inverter. Related issues are now discussed, before structuring a direct grid-current scheme for the differential boost inverter.

First, it should be emphasized that existing references [17], [18] have shown that grid current of a standard *LCL*-filtered full-bridge inverter can be regulated by a single control loop. Objective of the loop is to make the grid current track its reference $i_{g\text{ref}}$ precisely, and when that happens, tracking error $e_i$ in (15) will be zero in the steady state.

$$e_i = i_{g\text{ref}} - i_g. \tag{15}$$

Usually, the zeroing of $e_i$ may be ensured in either the synchronous or stationary frame. For the latter, it is guaranteed by the infinite gain of a proportional-resonant (PR) controller, whose undamped natural frequency must be set to the grid frequency. Output of the PR controller is then the duty ratio or modulating reference needed for performing pulsewidth modulation of the standard *LCL*-filtered full-bridge inverter.

The same single loop and PR controller may similarly be used with the differential boost inverter, since it is also *LCL*-filtered. They are therefore included in Fig. 7 as the main grid-current control block. It should however be emphasized that output of the PR controller need not necessarily be the duty ratio $d_j$. For example, in [11], output of the inner controller of a dual-mode scheme has been defined as the duty ratio $d_j$, but in [15], output of the inner controller of the double-loop CC-VC scheme has been treated as the inductor voltage $v_{Lj}$. As for the single-loop control strategy, output of the PR grid-current controller can either be the duty ratio $d_j$ or capacitor voltage $v_{Cj}$ of the differential boost inverter. To answer which parameter is better, values in Table I can be substituted into the first expression of (3), before substituting them into (5). The resulting expression is given in (16) shown at the bottom of this page, which shows that to produce the desired dc and fundamental ac components in (3) for the capacitor voltage $v_{Cj}$, the duty ratio $d_j$ must include second to fourth-order harmonics, in addition to the expected dc and fundamental ac components. Therefore, more resonant terms tuned at different natural frequencies will be needed for generating those harmonic control signals, if the controller is designed to output duty ratio $d_j$.

The additional resonant terms may be included by changing to a repetitive controller, which theoretically has been proven to represent an infinite sum of resonant terms. The tradeoffs are delay in response and loss of independent gain tuning for each resonant term. Nevertheless, repetitive control has been tried in [11], but mainly for compensating voltage harmonics when the differential boost inverter supplies a standalone nonlinear load without the grid. In other words, differences between capacitor voltage $v_{Cj}$ and duty ratio $d_j$ as a control signal generated by the grid-current controller have not been evaluated in [11].

Moreover, it should be emphasized that in Fig. 7, although third and a few odd resonant terms have been paralleled for compensating harmonics detected in the grid, the absence of even resonant terms does not permit duty ratio $d_j$ to be generated

$$1 - d_i = \frac{V_{\text{in}}}{v_{Cj}} \approx \frac{100}{230 + 77.5\sin(\omega_0 t)} \approx \frac{462 + 160\sin(\omega_0 t + 180^\circ) + 28\sin(2\omega_0 t - 90^\circ) + 5\sin(3\omega_0 t) + \sin(4\omega_0 t + 90^\circ)}{1000} \tag{16}$$

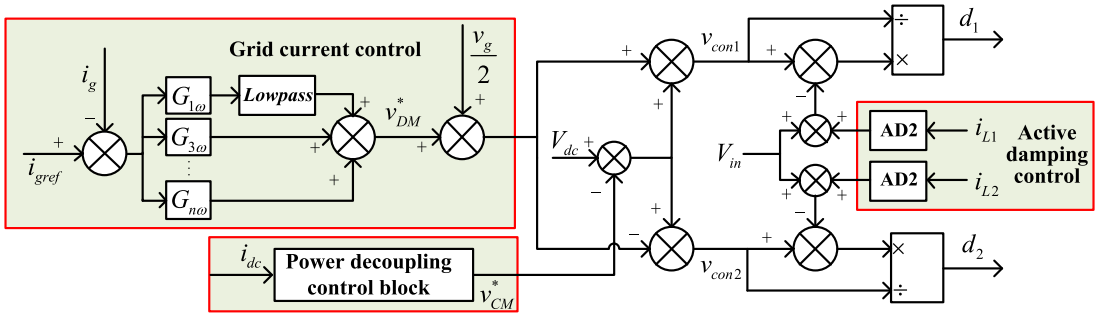


Fig. 7. Overall block diagram of proposed scheme.

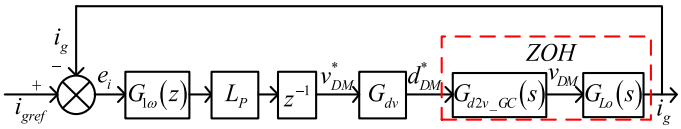


Fig. 8. Single-loop grid-current regulation.

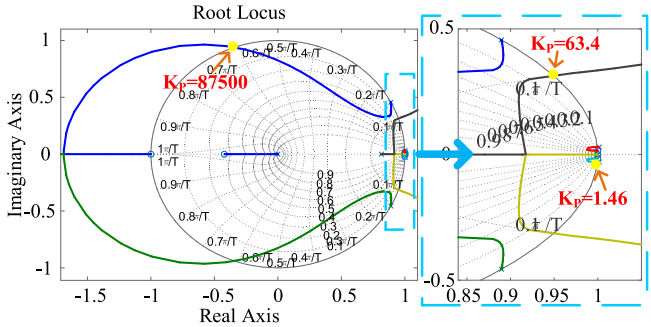


Fig. 9. Root locus of proposed grid-current regulation.

accurately by the grid-current controller, as understood from (16). Therefore, control signal $v_{\text{con}j}$ in Fig. 7 has been configured as the capacitor voltage $v_{Cj}$, which in the figure, is generated from the CM bias $V_{\text{dc}}$, measured grid voltage $v_g$ for phase-locking and controller output $v^*_{\text{DM}}$. More precisely, it can be expressed as

$$v_{\text{con}j} = V_{\text{dc}} + (-1)^{j-1}\left(\frac{v_g}{2} + G_c \cdot e_i\right) \tag{17}$$

where $G_c$ is the current controller assembled with $G_{1\omega}$, $G_{3\omega}$ up to $G_{n\omega}$.

Where necessary and as indicated in Fig. 7, a low-pass filter may also be inserted after the fundamental resonant term $G_{1\omega}$ [19]. Its purpose is to damp the higher resonance in Fig. 5, which means its cutoff frequency must be set smaller than the minimum of $\omega_{reH}$. The same low-pass filter should however not damp the lower resonance at $\omega_{reL}$, since it will severely compromise dynamics with an even lower cutoff frequency. Resonance damping at $\omega_{reL}$ is thus realized through another method to be discussed later, since it is external of the single grid-current loop.

Meanwhile, with $v_{\text{con}j}$ computed using (17), the required duty ratio $d_j$ can be computed with (18). Note that in (5), the dc inductor voltage $v_{Lj}$ has been neglected in (18), since it is much smaller than $V_{\text{in}}$ and has sizable amount of switching noises which make its sensing difficult.

$$d_j = \frac{v_{\text{con}j} - V_{\text{in}}}{v_{\text{con}j}}. \tag{18}$$

The full single grid-current loop with one-sample delay $z^{-1}$, low-pass filter $L_P$, and $G_{dv}$ for representing correlation between the DM capacitor voltage and duty ratio can then be represented in Fig. 8. Also shown in the figure are the inverter plant functions $G_{d2v\_\text{GC}}$ and $G_{Lo}$, whose expressions are obtained from (6) and (19) after small-signal linearization.

$$G_{Lo}(s) = 1/sL_o. \tag{19}$$

Similar linearization can also be applied to (5), which upon simplification, leads to the following $G_{dv}$ gain for correlating DM capacitor voltage and duty ratio:

$$G_{dv} = \frac{\hat{d}_j}{\hat{v}_{Cj}} = \frac{(1 - D)}{V_C}. \tag{20}$$

Open-loop transfer function for relating grid current $i_g$ to its error $e_i$ in Fig. 8 can then be expressed as

$$G_{ig\_op}(z) = \frac{i_g}{e_i} = G_{1\omega}(z)\, L_P z^{-1} G_{dv} Z_{\text{ZOH}}\left[G_{d2v\_\text{GC}}(s)\, G_{Lo}(s)\right] \tag{21}$$

from which closed-loop transfer function of the single grid-current loop can be derived as

$$G_{ig\_cl}(z) = \frac{G_{ig\_op}(z)}{1 + G_{ig\_op}(z)}. \tag{22}$$

Setting an initial resonant gain of 1630 and varying proportional gain of the PR grid-current controller permits root locus of the single grid-current loop to be plotted in Fig. 9, from which stable regions can clearly be identified. It is thus possible to stabilize the differential boost inverter, even though its stable regions can further be widened by including a virtual resistive scheme for damping the lower resonance in Fig. 5. Details of this damping scheme are discussed later. Meanwhile, a proper set of proportional and resonant gains for the PR grid-current controller $G_{1\omega}$ in Fig. 8 should be defined, based on a desired phase margin.

For that, Bode diagram of the single grid-current loop in Fig. 8 is plotted in Fig. 10, where its first peak at 50 Hz is due

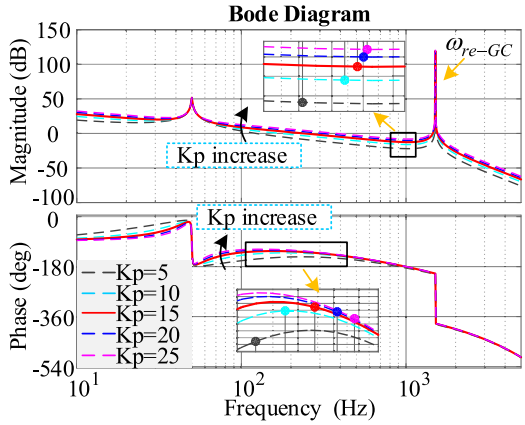


Fig. 10. Open-loop Bode diagram of single grid-current control loop obtained with different $K_p$.

to the PR controller $G_{1\omega}$. In contrast, the second peak is due to resonance at

$$\omega_{\mathrm{re-GC}} = \sqrt{\frac{L_o/2 + L/(1-D)^2}{(L_o/2)\,C\left[L/(1-D)^2\right]}}. \tag{23}$$

It is caused by all three components $L_o/2$, $C$, and $L/(1-D)^2$ in each hidden *LCL* filter, and is found to correspond to $\omega_{reH}$ in (13) at the assumed quiescent operating point for small-signal analysis. This resonance will destabilize the system, if the low-pass filter $L_p$ is not included. Additionally, it should be mentioned that the other resonance in (14) is not seen in Fig. 10, but will appear in Bode diagram plotted later for the power-decoupling control loop.

The next task is then to choose proper gains for the PR controller, based on the defined phase-margin. The process is the same as for a standard grid-tied inverter explained in [20]. It begins by plotting various open-loop frequency responses in Fig. 10, using different proportional gains. The plot then shows an increasing phase margin caused by an increasing proportional gain until a certain critical gain. Above this gain, the phase margin starts to decrease. Other observations noted are the continuous decrease of gain margin and strengthening of resonance magnitude, as the proportional gain increases. The proportional gain has hence been limited to $K_p = 15$ for a phase margin of 50° (reduced $K_p = 12$ used for experiment to cater for practical variations of passive parameters). This then leads to a resonant gain of [20], [21]

$$K_r = \frac{K_p \omega_c}{10} = 2300 \tag{24}$$

where $\omega_c$ is the unity-gain crossover frequency.

## IV. Auxiliary Control Strategies for Performance Improvement

After finalizing the single direct grid current loop, auxiliary control strategies for power decoupling and active damping can be added for further improving qualities of dc input current and grid current. These control additions are described as follows.

### A. Power Decoupling

As commonly known, instantaneous power of any single-phase inverter has a second-order harmonic, which if supplied directly by the dc source, may progressively damage it. It may therefore be desirable to divert the second-order harmonic away from the dc source. For the symmetrical differential boost inverter in Fig. 1, it may be diverted to capacitors $C_1$ and $C_2$, which according to [10] and [11], will require a CM second-order component to be added to the two capacitor voltages in (3). This second-order voltage has however been inefficiently generated in [10] and [11]. Explanation for that can be deduced from Fig. 11, where the first observation noted is the summation of the two dc inductor currents $i_{L1}$ and $i_{L2}$ to obtain $i_{\mathrm{dc}}$ supplied by the dc source. Current $i_{\mathrm{dc}}$ is then high-pass filtered to remove its dc component, before passing it through resonant terms at specified natural frequencies. These resonant terms will simply force harmonics of $i_{\mathrm{dc}}$ to zero at those natural frequencies.

Outputs of the resonant terms are then summed, and may be introduced to the single grid-current control loop at any of the three positions, marked as PDC1, PDC2, and PDC3 in Fig. 11. In [11], only PDC2 has been considered, where the summed output of power decoupling has been viewed as a component of duty ratio. But, because of the same reason explained with (16), it will unnecessarily demand more resonant terms to generate each CM harmonic voltage across the capacitors. In contrast, PDC1 requires only one resonant term to generate each CM harmonic voltage directly. It is thus preferred and included in the overall control scheme shown in Fig. 7. Control signal $v_{\mathrm{con}j} \approx v_{Cj}$ in (17) then changes to

$$v_{\mathrm{con}j} = V_{\mathrm{dc}} + (-1)^{j-1}\left(\frac{v_g}{2} + G_c \cdot e_i\right) - v^*_{\mathrm{CM}} \tag{25}$$

where $v^*_{\mathrm{CM}}$ represents the CM capacitor voltage produced by PDC1.

Although PDC3 has also been marked in Fig. 11 (and verified to work fine in experiment), it is not a favorable option, which can be demonstrated by first noting that its summed output has been treated as an extra dc inductor voltage. The applicable duty-ratio expression is thus (4), since the dc inductor voltage is no longer small, and hence cannot be ignored. Applying small-signal analysis to (4) then results in

$$\Delta v_{Lj} = \Delta d_j \cdot V_C - \Delta v_{Cj} \cdot (1 - D) \tag{26}$$

where the presence of three perturbed parameters prevents the formulation of a transfer function for relating a single perturbed input to a single perturbed output. PDC3 is therefore not as straightforward to analyze using classical control tools.

Returning to the chosen PDC1 scheme, its full power-decoupling control loop is shown in Fig. 12(a). It includes the usual one-sample delay $z^{-1}$, $G_{dv}$ from (20), $G_{d2i\_\mathrm{PD}}$ from (7), PR controller $G_{\mathrm{PD}}$, and the mentioned high-pass filter $H_P$ with a cutoff frequency of 1.5 Hz for removing dc component from the input current. The PR controller $G_{PD}$ must additionally be tuned to the second-order harmonic frequency, as indicated by the first peak of the open-loop Bode diagram plotted in Fig. 12(b). Proportional and resonant gains used with the diagram are $K_{p,\mathrm{PD}} = 5$ and $K_{r,\mathrm{PD},100\,\mathrm{Hz}} = 800$, respectively, for

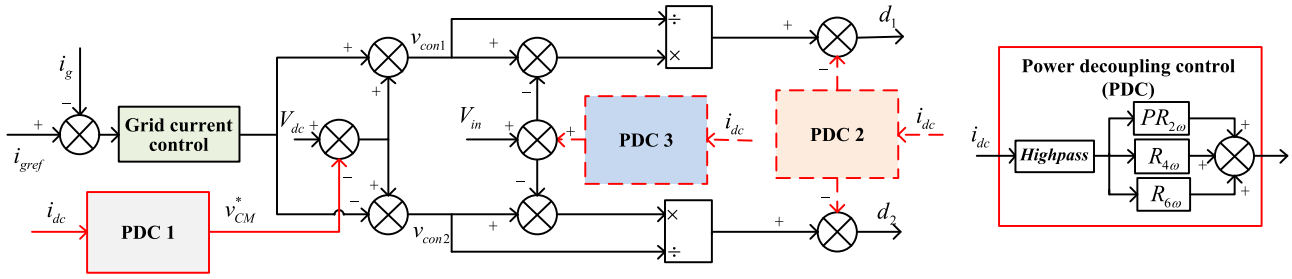


Fig. 11. Illustration of various power decoupling options.

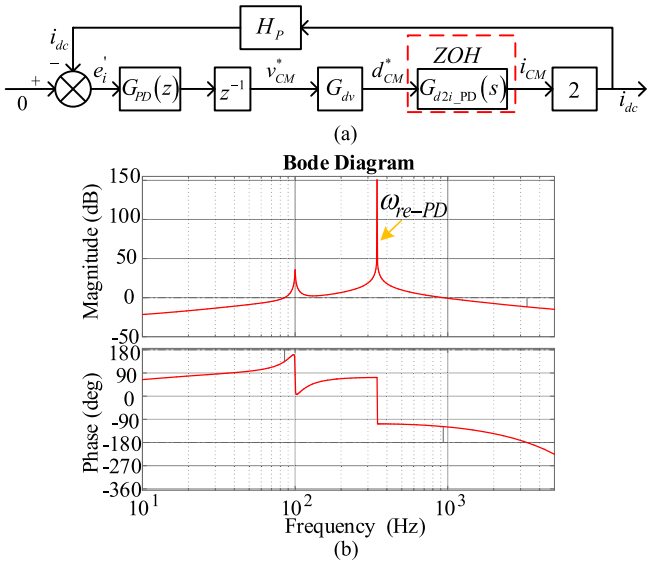


Fig. 12. Illustration of (a) control blocks within power-decoupling loop and (b) its accompanied open-loop Bode diagram.

enforcing a phase margin of around 45° [22] (reduced $K_{p,\mathrm{PD}} = 4$ used for experiment to cater for practical variations of passive parameters). The second peak in the diagram has also been analyzed and identified as a resonance at

$$\omega_{\mathrm{re-PD}} = \sqrt{\frac{1}{C\left[L/(1-D)^2\right]}}. \tag{27}$$

This resonance corresponds to $\omega_{reL}$ from (14) at its assumed quiescent operating point with duty ratio $D$. It is introduced by capacitance $C$ and inductance $L/(1-D)^2$ within each hidden *LCL* filter. In other words, the grid inductance is not seen by the power-decoupling control loop, which processes only CM quantities [11]. Additionally, Fig. 12(b) suggests that although frequency of this resonance is low, its phase roll-off does not cause phase along the forward control path to transit below −180°. Therefore, the power-decoupling control loop does not influence system stability, and can merely be designed by enforcing a phase margin of 45°, as done in this section. Other resonant gains for attenuating the fourth and sixth harmonics can then be set as $K_{r,\mathrm{PD,200\ Hz}} = 100$ and $K_{r,\mathrm{PD,\ 300\ Hz}} = 10$, which are factors of 8 and 80 smaller than $K_{r,\mathrm{PD,100\ Hz}}$. These extra gains are generally less critical, since the fourth and sixth harmonics are usually much smaller than the second-order harmonic.

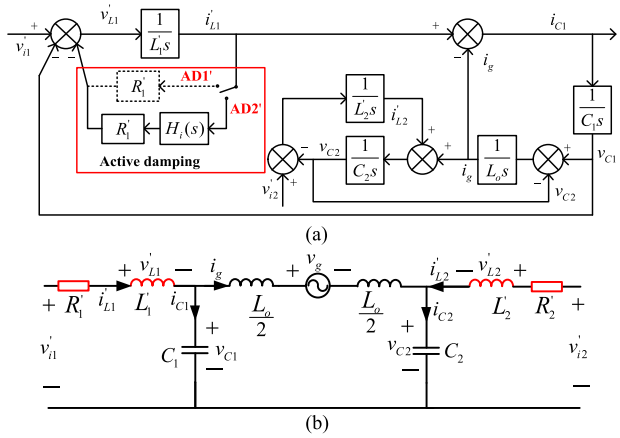


Fig. 13. Proposed active resistive damping illustrated as (a) control block diagram and (b) equivalent circuit with hidden *LCL* filters.

## B. Active Resistive Damping

Existing damping schemes for the standard *LCL*-filtered full-bridge inverter have mostly depended on the feedback of either grid current or capacitor current [23], [24]. According to circuit laws, these parameters can further be related to the immediate inductive current flowing out of the full-bridge inverter. It may hence be considered as the third possible feedback parameter, which has more commonly been emphasized with double-loop control for power supplies [25], rather than single grid-current loop. There are hence three possible currents that can be fed back for damping, and they are all ac parameters for the standard *LCL*-filtered full-bridge inverter.

Likewise, for the differential boost inverter with hidden *LCL* filters, there are three parameters, and they are $i_g$, $i_{Cj}$ and $i'_{Lj}$ in Fig. 2. Current $i'_{Lj}$ is however a reflected parameter, which can greatly help with analysis, but can only be sensed in its original dc frame. The differential boost inverter therefore has two prospective feedback terms $i_g$ and $i_{Cj}$ in its ac frame and one term $i_{Lj}$ (without′) in its dc frame. The eventual decision is to feed back the dc inductor current $i_{Lj}$ for damping, since it is needed for power decoupling simultaneously, as demonstrated in the earlier subsection.

Meanwhile, damping with $i_{Lj}$ feedback can be designed with reflected parameters and those enclosed control blocks shown in Fig. 13(a) for one of the two dc–dc converters inside the differential boost inverter. Assuming now that path AD1′ in the figure is enabled, proportional term $R'_1$ will then be inserted to the equivalent circuit as a series reflected resistance, such

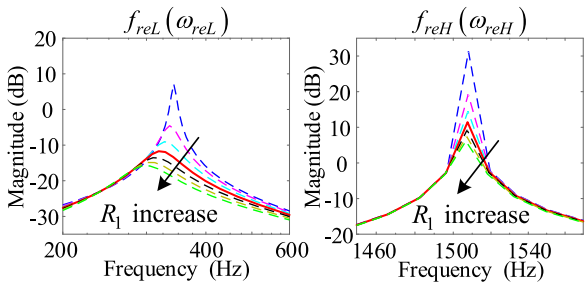


Fig. 14. Bode diagram of $i_{Cj}/v'_{ij}$ plotted with different $R_1 = 0.1$, 0.4, 0.7, 1, 1.3, 1.6, and 1.9 Ω.

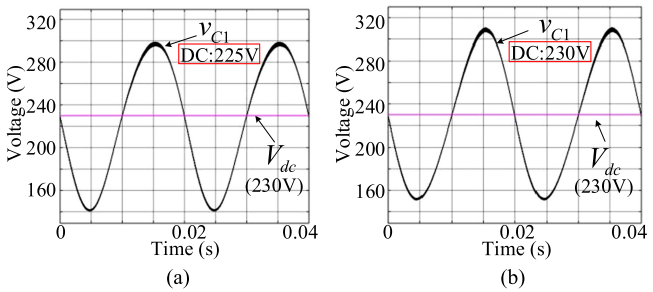


Fig. 15. Simulated capacitor voltage (a) without and (b) with high-pass filter along active damping path.

as in Fig. 13(b). This reflected resistance can be expressed as $R'_1 = R_1/(1-d_1)^2$, where $R_1$ is the virtual resistance inserted at the dc side through feeding back the actual dc inductor current $i_{L1}$. Value of $R'_1$ should additionally be positive, and always bigger in magnitude than the negative minimum value of $r'_1$, which as explained earlier, is a resistance unintentionally created by reflecting inductance $L_1$ from the dc to ac frame.

Mathematically, it can be expressed as $R'_{j,\min} \geq |r'_j|_{\max}$, and then $R_{j,\min} \geq |\frac{L_j}{1-d_j}\frac{d(d_j)}{dt}|_{\max}$, where subscripts *min* and *max* are for representing minimum and maximum values, respectively, and $j = 1$ or 2 are for representing the two dc–dc boost converters. The specific minimum damping resistance can then be determined as $R_{j,\min} \geq 0.097\ \Omega$, after plotting $r_j = \frac{L_j}{1-d_j}\frac{d(d_j)}{dt}$ in Fig. 3(b) using parameters provided in Table I. This minimum resistance is however only a guideline, since the actual resistance adopted usually depends on the amount of damping preferred. For demonstrating that, magnitude responses of $i_{Cj}/v'_{ij}$ have been plotted in Fig. 14 for showing how magnitudes of both resonances at their respective smallest frequencies decrease, as $R_j$ increases. The drops in magnitudes have however become less significant, as $R_j$ increases beyond 1 Ω. This trend has also been observed with damping of a standard grid-connected inverter [26], [27]. It is thus justifiable to set $R_j = 1\,\Omega$, in case of damping through feeding back the actual dc inductor current $i_{Lj}$.

Limiting $R_j$ (to 1 Ω), and hence $R'_j$ in Fig. 13(b) can additionally prevent unintentional drops of capacitor voltages $v_{Cj}$ at all frequencies, including at dc. To illustrate, Fig. 15(a) shows $v_{C1}$, whose average value has obviously been shifted slightly below the specified dc bias of $V_{\rm dc}$. This may cause $v_{C1}$ to unintentionally drop below input voltage $V_{\rm in}$, and its associated dc–dc boost converter to malfunction, if the ac component of $v_{C1}$ is close to $V_{\rm dc}$. It is thus desirable to remove the resistive voltage drop, at least at low-order frequencies, where current components may be high.

The recommendation is thus to include an extra high-pass filter $H_i(s) = s/(\tau s + 1)$, as demonstrated along path AD2′ in Fig. 13(a). Cutoff frequency of this filter must be below the smallest lower resonance peak $\omega_{reL}$ in Fig. 5 to ensure that damping is effective at all possible resonance frequencies. In other words, damped magnitude responses in Fig. 14 are still applicable. The cutoff frequency is thus set as 150 Hz, which will, in turn, reduce virtual resistive voltage drop below that frequency, especially at dc. An illustration for demonstrating it can be found in Fig. 15(b), where $v_{C1}$ is now more centrally placed along $V_{\rm dc}$. Path AD2′ is therefore preferred for enforcing resonance damping in Fig. 14, while limiting resistive drops at low-order frequencies. It should however be noted that magnitude of the higher resonance in Fig. 14 is still larger than that of the lower resonance. The higher resonance should hence be further be damped by the low-pass filter $L_P$, placed in the grid-current control loop, as indicated in Figs. 7 and 8.

Particularly, in Fig. 7, where the overall proposed scheme has been drawn, the active resistive damping AD2 blocks have also been included, through which the actual dc inductor currents $i_{L1}$ and $i_{L2}$ pass. The common gain of these blocks must hence be $R_1 = R_2 = R$, set as a constant (of 1 Ω), rather than those reflected resistances $R'_1$ and $R'_2$ analyzed in Fig. 13. But, in Fig. 13(b), both resistances $R_1$ and $R_2$ must, respectively, be in series with the dc inductors $L_1$ and $L_2$, which are also in series with the input dc source $V_{\rm in}$. Outputs of the two AD2 blocks in Fig. 7 must therefore be, respectively, added to $V_{\rm in}$ to approximately obtain voltages that the two dc–dc boost converters must generate at their immediate low-voltage terminals to emulate these series connections.

## V. Simulation and Experimental Results

To validate the designed control scheme, a differential boost inverter has been simulated and built. Its circuit configuration is like shown in Fig. 1 with parameters provided in Table I. Additionally, its modulation has been interleaved like the one given in [11], where the two triangular carriers of the two dc–dc constituting converters have been shifted by 180° to shift their respective current ripples in $i_{L1}$ and $i_{L2}$ in Fig. 1 by the same amount. Current $i_{\rm dc}(= i_{L1} + i_{L2})$ drawn from the dc input source will then have a smaller ripple. Results obtained are now described, as follows.

### A. Verification of Varying Resonance Frequencies

Resonances predicted by the equivalent model with two hidden *LCL* filters in Fig. 2 cannot be safely verified in experiment, because of large current flow. The differential boost inverter in Fig. 1 has thus been simulated in MATLAB, using duty ratio that varies according to (16). Results obtained are provided in Fig. 16, where large resonances can be seen in each 20-ms fundamental period of the input current $i_{\rm dc}$, grid current $i_g$, and one

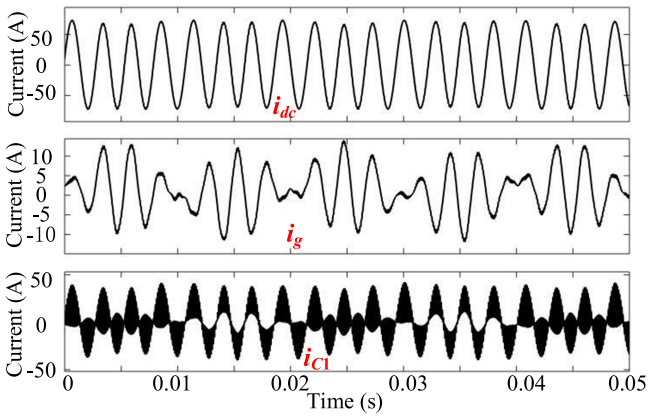


Fig. 16. Simulated waveforms with open-loop supply of duty ratio in (16).

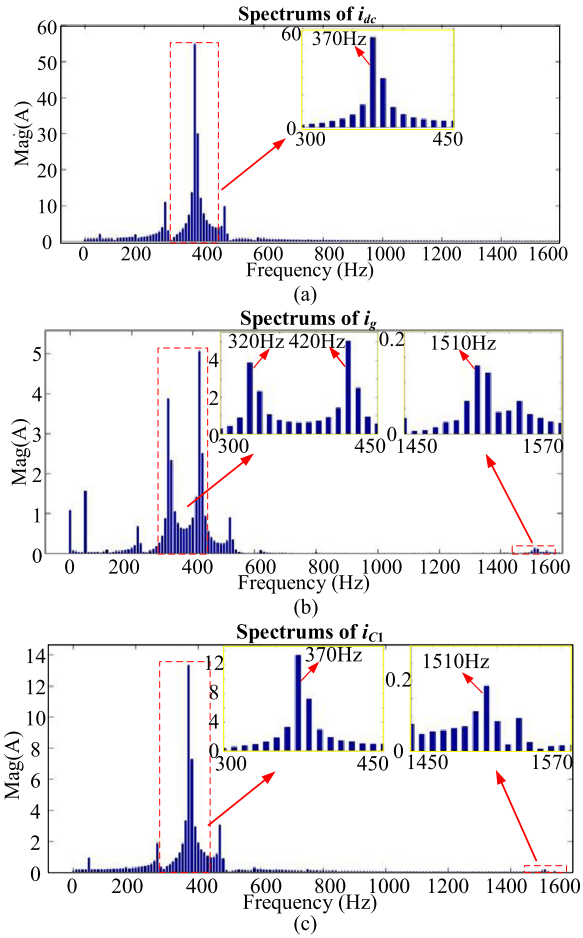


Fig. 17. Spectrums of (a) input, (b) grid, and (c) capacitor currents.

of the capacitor currents $i_{C1}$. Particularly, for $i_{C1}$, Fig. 5 informs that its lower resonance frequency band should be between 344 and 404 Hz, whereas its higher resonance band should be between 1510 and 1530 Hz. To verify, simulated spectrum of $i_{C1}$, obtained through fast Fourier transform, is shown in Fig. 17(c), where resonance peaks have clearly been noted to occupy both predicted bands. Magnitudes of the resonance peaks in each band are however different, because of the third varying resistive term in (11), which has not been considered in Fig. 5. This varying resistive term may also cause damped frequencies of the resonance peaks to divert slightly from their undamped values.

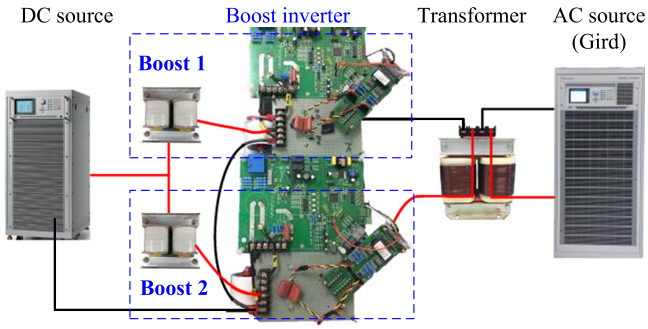


Fig. 18. Experimental prototype of differential boost inverter.

Other features, that may be unmasked, are from spectrums plotted for $i_{\rm dc}$ and $i_g$ in Fig. 17(a) and (b), and their comparison with $i_{C1}$ in Fig. 17(c). The comparison has, in fact, revealed that most lower resonance peaks of $i_{C1}$ are from $i_{\rm dc}$, whereas most of its higher resonance peaks are from $i_g$. This may be related to $i_{C1}$ being the intermediate current between input $i_{\rm dc}$ and output $i_g$. Moreover, since $i_{\rm dc}$ and $i_g$ are at different sides of the inverter, their interaction will result in new resonance peaks. For example, in Fig. 17(a), a component of $i_{\rm dc}$ at 370 Hz will cause corresponding components of $i_g$ to appear at (370 $\pm$ 50) Hz, as confirmed by Fig. 17(b). Similarly, a component of $i_g$ at 1510 Hz will cause corresponding components of $i_{\rm dc}$ to appear at (1510 $\pm$ 50) Hz. These components are however too small, and hence not noticeable in Fig. 17(a).

### B. Experimental Results Obtained With the Proposed Scheme

Effectiveness of the proposed scheme has next been validated with the experimental prototype shown in Fig. 18, where the proposed scheme has been implemented with a dSPACE DS1005 controller board using control and circuit parameters provided in Table I. Meanwhile, the differential boost inverter has been assembled with insulated gate bipolar transistors IHW40T60 from Infineon. Subsequently, the inverter has been powered by a *Chroma 61511* dc supply, whose energy has been channeled through the inverter to a *Chroma 61830 Regenerative AC Grid Simulator*. Since the grid simulator can both supply and absorb power, an external ac load for sinking power from the differential inverter has not been included, but as an extra precaution, a step-up transformer found in the laboratory has been inserted between the inverter and simulator.

Leakage inductance at the low-voltage side of the transformer seen by the inverter has then been measured as 0.5 mH, which in the experiment, has been regarded as the grid inductance. This grid inductance, together with other inductances and capacitances provided in Table I, has caused the higher resonance to narrowly vary around $\omega_{reH} = 1515$ Hz, as read from Fig. 5. Cutoff frequency of the low-pass filter in Fig. 7 has hence been set to 636 Hz for damping this resonance, while not over-limiting the grid-current control bandwidth. As for the lower resonance at $\omega_{reL}$, it can be damped by enabling the proposed active damping

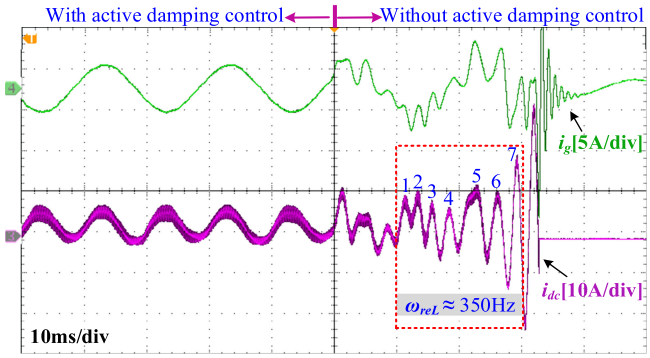


Fig. 19. Experimental results of proposed scheme with and without active damping control.

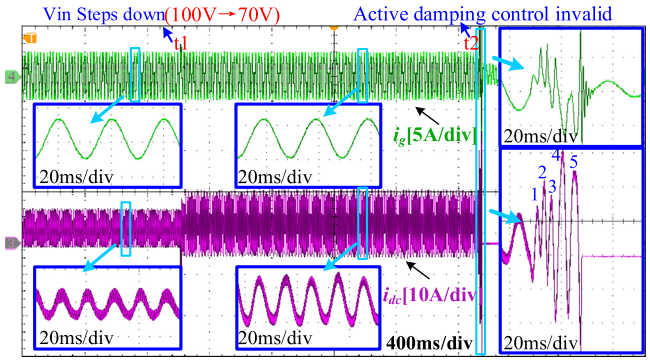


Fig. 20. Experimental results of proposed scheme when dc voltage was stepped from 100 to 70 V.

scheme. Experimental results obtained are provided in Fig. 19, where active damping has initially been enabled, before being disabled somewhere in the middle of the diagram (power decoupling not yet introduced). Clearly, removal of damping has triggered oscillation, whose magnitude may theoretically become infinite, if circuit resistance is ideally zero.

The increasing oscillation has subsequently activated hardware protection, which has hence made it impossible to capture enough steady-state cycles for spectral analysis. Therefore, frequency of the oscillation has roughly been determined by counting the number of cycles after disabling damping, which for the dc current, gives 350 Hz. The estimated value is thus close to 370 Hz read from Fig. 17(c) and within the range of $\omega_{reL}$ read from Fig. 5. Irrespective of that, resonance at the higher frequency of $\omega_{reH}$ cannot be noticeably determined from Fig. 19, since it has been more prominently damped by circuit resistance at a higher frequency. Its magnitude is thus much smaller.

To next demonstrate how resonance varies with input voltage $V_{\text{in}}$, its value has been dropped from 100 to 70 V at time instant $t1$ in Fig. 20 (power decoupling not yet enabled). The drop has obviously not caused any abnormality until $t2$, at which damping has been disabled. Abnormal ever-increasing oscillation has since been triggered until near the end of the figure, at which hardware protection has been activated. Like earlier, the number of oscillating cycles has then been counted to roughly determine the resonance frequency as 250 Hz, which is correctly within the new range of $\omega_{reL}$, read from Fig. 6 when $V_{\text{in}} = 70$ V. The other resonance at $\omega_{reH}$ has however not been measurable like before, since its magnitude has been more significantly damped by circuit resistance at a higher frequency. Despite that, both Figs. 19 and 20 have confirmed that the proposed damping scheme is essential to the inverter, whose performance can further be enhanced by enabling power decoupling.

To demonstrate it, Fig. 21(a) and (b) show waveforms obtained without and with power decoupling. Indifferently, they confirm that grid-current $i_g$ is sinusoidal, but it is only in Fig. 21(b) with power decoupling enabled that has caused the dc input current $i_{\text{dc}}$ to be freed from second-order and other even-multiple harmonics. These observations have been confirmed by spectrums plotted in Fig. 22, where Fig. 22(a) shows THD of $i_g$ to be around 1.6% and its harmonics from second to tenth order to be less than 1% each without and with power decoupling. Enabling power decoupling however permits the sizable second-order harmonic and other even-multiple harmonics in $i_{\text{dc}}$ to be reduced significantly, as seen from Fig. 22(b).

Dynamic performance of the proposed scheme has also been tested with its results shown in Fig. 23 for an increase in grid current from 1 to 3 A, and then the reverse. The results confirm that the scheme will stabilize in around two line cycles, even though the target controlled is the dynamically more challenging differential boost inverter, rather than standard full-bridge inverter. From all experiments, it has also been noticed that no prominent circulating current flows between the two constituting dc–dc converters, except for the fundamental grid current. Theoretically, circulating current may flow, whose magnitude depends on the extent of mismatch between parameters of the two constituting converters. Related issues and solutions have earlier been studied in [28] for a differential buck inverter, whose findings are equally applicable to the differential boost inverter. Those findings are however not included here, since no prominent circulating current has been observed from all experiments.

### C. Experimental Results Obtained With the CC-VC Scheme

To further project improvements offered by the proposed scheme, experiments have been performed with the CC-VC scheme using the same number of resonant controllers as in [15] to keep low-order harmonics within standard grid codes. The CC-VC scheme has been chosen here, because it can also control the grid current directly, whereas other existing schemes mainly provide voltage regulation to standalone loads. Waveforms obtained with the CC-VC scheme are thus provided in Fig. 24(a) without power decoupling and Fig. 24(b) with power decoupling for comparison. The comparison confirms that waveforms of $i_g$ and $i_{\text{dc}}$ produced by the CC-VC scheme are visibly more distorted. Their levels of distortion can better be analyzed from Fig. 22, where their spectrums are plotted besides those of the proposed scheme.

Undeniably, Fig. 22(a) confirms that the CC-VC scheme can keep THD of $i_g$ and its second to tenth-order harmonics within the requirements of IEEE 1547 standard when power decoupling is disabled. They are however not as low as those offered by the proposed scheme, because of an approximated voltage

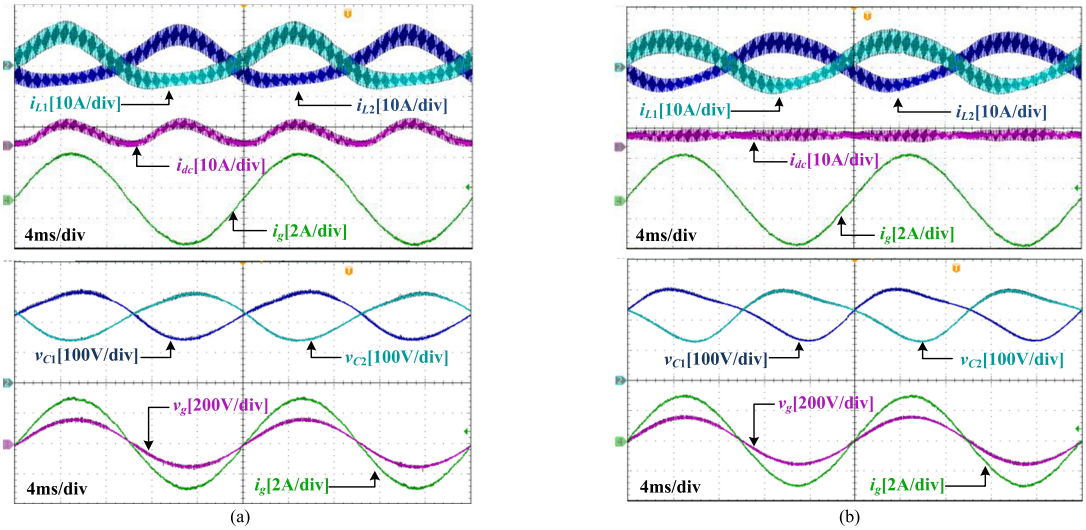


Fig. 21. Experimental results of proposed scheme obtained (a) without and (b) with power decoupling.

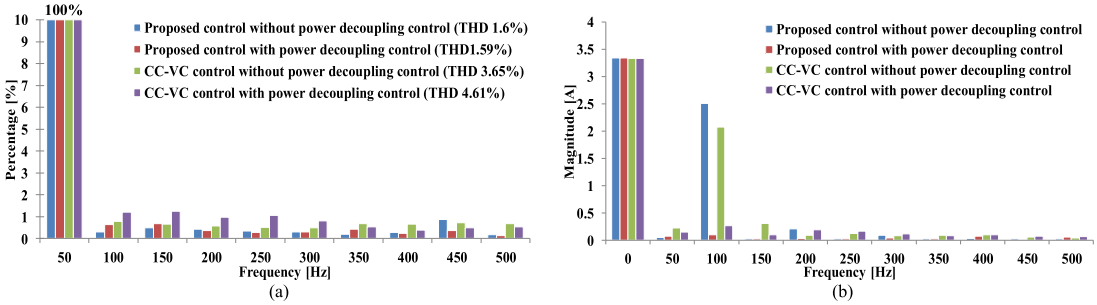


Fig. 22. Summarized spectrums of (a) grid and (b) input currents.

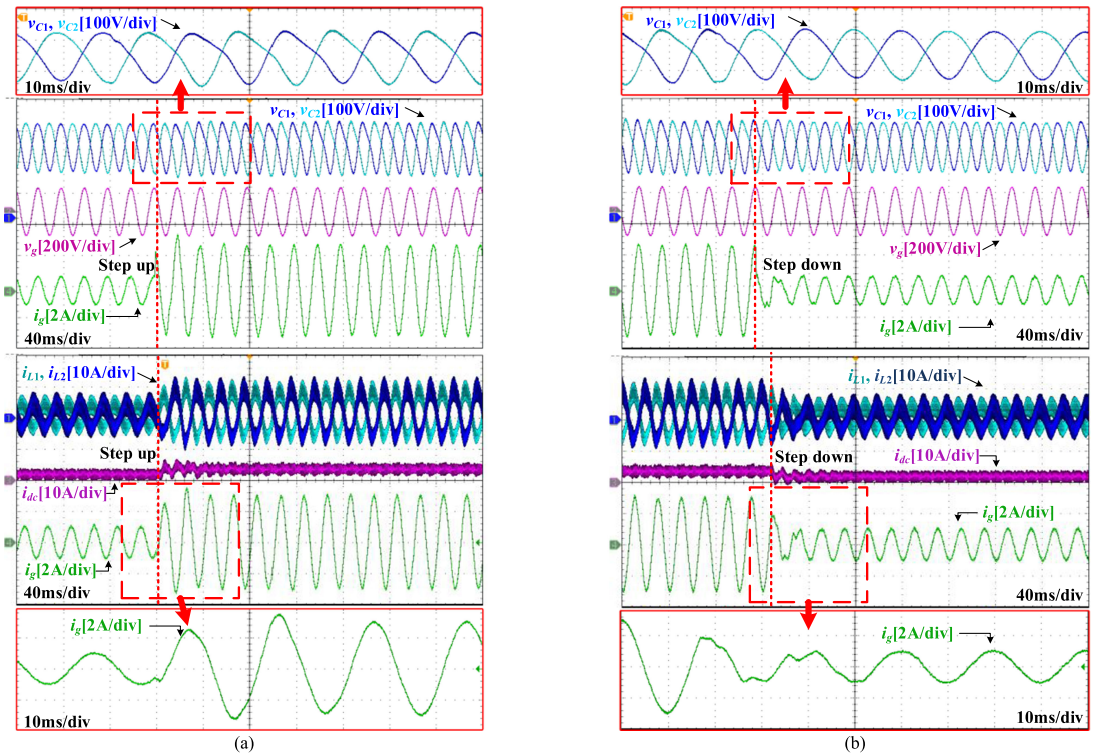


Fig. 23. Experimental results of proposed scheme when $i_{g\,\mathrm{ref}}$ steps from (a) 1 to 3 A and (b) 3 to 1 A.

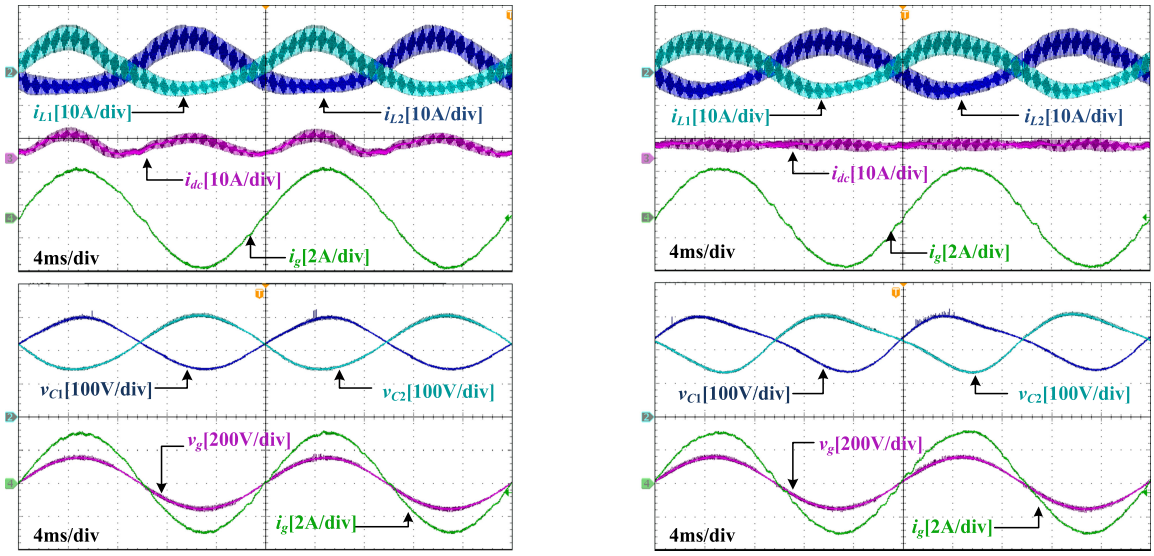


Fig. 24. Experimental results of CC-VC scheme (a) without and (b) with power decoupling.

reference adopted by the CC-VC scheme. To explain, it should be recapped that the CC-VC scheme controls only one dc–dc boost converter to regulate the grid current [15]. The second dc–dc boost converter then has its capacitor voltage regulated to follow an approximated reference, expressed by $v_{C2}$ in (28) in the appendix without considering power decoupling yet. Accordingly to circuit laws, capacitor voltage generated by the first dc–dc boost converter must then be $v_{C1}$ in (28), even though it is grid-current regulated. The two capacitor voltages are thus asymmetrical, which together, lead to fundamental and second-order input current harmonics in (29), derived using mathematical procedure outlined in [6].

These harmonics further yield other even and odd-multiple harmonics, after undergoing interaction between ac and dc sides of the inverter. It thus explains why spectrum of $i_{\rm dc}$ associated with the CC-VC scheme in Fig. 22(b) contains both even- and odd-multiple harmonics. The even-multiple harmonics can promptly be reduced by enabling power decoupling, which as per earlier, requires a second-order CM voltage reference to be added to $v_{C2}$ in (28) for tracking by the second dc–dc boost converter. This second-order voltage reference is however not symmetrically generated in $v_{C1}$ by the first dc–dc boost converter, because of voltage $v_{L0}$ across the grid inductance. Incomplete cancellation of second-order CM voltage between $v_{C1}$ and $v_{C2}$ thus exists. The outcomes are an even more distorted grid current spectrum in Fig. 22(a) and an observable amount of retained odd input current harmonics in Fig. 22(b), after enabling power decoupling with the CC-VC scheme. In contrast, the proposed scheme is symmetrical, and will hence not be burdened by odd-multiple harmonics and incomplete cancellation of CM capacitor voltage.

## VI. Conclusion

A single grid-current loop with virtual resistive damping and power decoupling has been proposed for a single-phase differential boost inverter with two hidden *LCL* filters. These filters may first be analyzed by reflecting dc inductances to the ac frame. The reflected equivalent model then exhibits two resonances, whose frequencies vary with the inverter duty ratios over two determinable ranges. Damping of these resonances may however still be ensured by feeding back the dc inductor currents, which nevertheless have already been fed back for power decoupling. Other damping parameters have therefore not been recommended. Moreover, through analyzing number of necessary resonant terms, control signals from the grid-current and power decoupling controllers have been chosen to represent capacitor voltages, rather than duty ratios or other parameters. These considerations, upon incorporated, lead to a single grid-current loop scheme with many improvements over the existing asymmetrical CC-VC scheme.

## Appendix

$$\begin{aligned} v_{C1} &= V_{\rm dc} + \frac{1}{2}V_g \sin(\omega_0 t) + v_{L0} \\ v_{C2} &= V_{\rm dc} - \frac{1}{2}V_g \sin(\omega_0 t) \end{aligned} \tag{28}$$

$$i_{\rm dc} = \frac{1}{V_{\rm in}} \left\{ \begin{aligned} &\frac{V_g \cdot I_g}{2} - \frac{V_g I_g}{2}\cos(2\omega_0 t) + \frac{C\omega_0 V_g^2}{4}\sin(2\omega_0 t) \\ &+ \frac{C}{2}V_g \frac{dv_{L0}}{dt}\sin(\omega_0 t) + Cv_{L0}\frac{dv_{L0}}{dt} + CV_{\rm dc}\frac{dv_{L0}}{dt} \\ &+ v_{L0}\left\{ I_g \sin(\omega_0 t) + \frac{C\omega_0 V_g}{2}\cos(\omega_0 t) \right\} \end{aligned} \right. \tag{29}$$

where $v_{L0}$ is voltage drop across the grid inductance.

## REFERENCES


[1] F. Blaabjerg, Z. Chen, and S. B. Kjaer, "Power electronics as efficient interface in dispersed power generation systems," *IEEE Trans. Power Electron.*, vol. 19, no. 5, pp. 1184–1194, Sep. 2004.

[2] K. Li, Y. Hu, and A. Ioinovici, "Generation of the large DC gain step-up nonisolated converters in conjunction with renewable energy sources starting from a proposed geometric structure," *IEEE Trans. Power Electron.*, vol. 32, no. 7, pp. 5323–5340, Jul. 2017.

[3] A. Sangwongwanich, Y. Yang, and F. Blaabjerg, "A sensorless power reserve control strategy for two-stage grid-connected PV systems," *IEEE Trans. Power Electron.*, vol. 32, no. 11, pp. 8559–8569, Nov. 2017.

[4] R. J. Wai, M. W. Chen, and Y. K. Liu, "Design of adaptive control and fuzzy neural network control for single-stage boost inverter," *IEEE Trans. Ind. Electron.*, vol. 30, no. 12, pp. 7282–7298, Sep. 2015.

[5] R. O. Caceres and I. Barbi, "A boost DC-AC converter: Analysis, design, and experimentation," *IEEE Trans. Power Electron.*, vol. 14, no. 1, pp. 134–141, Jan. 1999.

[6] G. R. Zhu, S. C. Tan, Y. Chen, and C. K. Tse, "Mitigation of low-frequency current ripple in fuel-cell inverter systems through waveform control," *IEEE Trans. Power Electron.*, vol. 28, no. 2, pp. 779–792, Feb. 2013.

[7] G. R. Zhu, C. Y. Xiao, H. R. Wang, and S. C. Tan, "Closed-loop waveform control of boost inverter," *IET Power Electron*., vol. 9, pp. 1808–1818, Mar. 2016.

[8] S. Li, G. R. Zhu, S. C. Tan, and Y. S, "Direct AC/DC rectifier with mitigated low-frequency ripple through inductor-current waveform control," *IEEE Trans. Power Electron.*, vol. 30, no. 8, pp. 4336–4348, Aug. 2015.

[9] D. B. W. Abeywardana, B. Hredzak, and V. G. Agelidis, "A rule-based controller to mitigate DC-side second-order harmonic current in a single-phase boost inverter," *IEEE Trans. Power Electron.*, vol. 31, no. 2, pp. 1665–1679, Feb. 2016.

[10] D. B. W. Abeywardana, B. Hredzak, and V. G. Agelidis, "An input current feedback method to mitigate the DC-side low frequency ripple current in a single-phase boost inverter," *IEEE Trans. Power Electron.*, vol. 31, no. 6, pp. 4594–4603, Jun. 2016.

[11] N. Lu, S. Yang, and Y. Tang, "Ripple current reduction for fuel cell powered single-phase uninterruptible power supplies," *IEEE Trans. Ind. Electron.*, vol. 64, no. 8, pp. 6607–6617, Aug. 2017.

[12] D. Cortes, J. Alvarez, J. Alvarez, and A. Fradkov, "Tracking control of the boost converter," *IEE Proc. Control Theory Appl.*, vol. 151, no. 2, pp. 218–224, Mar. 2004.

[13] P. Sanchis, A. Ursaea, E. Gubia, and L. Marroyo, "Boost DC-AC inverter: A new control strategy," *IEEE Trans. Power Electron.*, vol. 20, no. 2, pp. 343–353, Mar. 2005.

[14] I. Purnama, P. C. Chi, Y. C. Hsieh, J. Y. Lin, and H. J. Chiu, "One cycle controlled grid-tied differential boost inverter," *IET Power Electron*., vol. 9, pp. 2216–2222, May. 2016.

[15] W. Zhao, D. D. C. Lu, and V. G. Agelidis, "Current control of grid-connected boost inverter with zero steady-state error," *IEEE Trans. Power Electron.*, vol. 26, no. 10, pp. 2825–2834, Oct. 2011.

[16] R. Ferrero, M. Marracci, and B. Tellini, "Single PEM fuel cell analysis for the evaluation of current ripple effects," *IEEE Trans. Instrum. Meas.*, vol. 62, no. 5, pp. 1058–1064, May. 2013.

[17] D. Pan, X. Ruan, X. Wang, H. Yu, and Z. Xing, "Analysis and design of current control schemes for LCL-type grid-connected inverter based on a general mathematical model," *IEEE Trans. Power Electron.*, vol. 32, no. 6, pp. 4395–4410, Jun. 2017.

[18] D. Pan, X. Ruan, C. Bao, W. Li, and X. Wang, "Capacitor- current-feedback active damping with reduced computation delay for improving robustness of LCL-type grid-connected inverter," *IEEE Trans. Power Electron.*, vol. 29, no. 7, pp. 3414–3427, Jul. 2014.

[19] J. Dannehl, M. Liserre, and F. W. Fuchs, "Filter-based active damping of voltage source converters with LCL filter," *IEEE Trans. Ind. Electron.*, vol. 58, no. 8, pp. 3623–3633, Aug. 2011.

[20] S. Parker, B. P. McGrath, and D. G. Holmes, "Regions of active damping control for LCL filters," *IEEE Trans. Ind. Appl.*, vol. 50, no. 1, pp. 424–432, Jan./Feb. 2014.

[21] D. G. Holmes, T. A. Lipo, B. P. McGrath, and W. Y. Kong, "Optimized design of stationary frame three phase AC current regulators," *IEEE Trans. Power Electron.*, vol. 24, no. 11, pp. 2417–2426, Nov. 2009.

[22] I. Serban, "Power decoupling method for single-phase h-bridge inverters with no additional power electronics," *IEEE Trans. Ind. Electron.*, vol. 62, no. 8, pp. 4805–4813, Aug. 2015.

[23] X. Wang, F. Blaabjerg, and P. C. Loh, "Virtual RC damping of LCL-filtered voltage source converters with extended selective harmonic compensation," *IEEE Trans. Power Electron.*, vol. 30, no. 9, pp. 4726–4737, Sep. 2015.

[24] X. Wang, F. Blaabjerg, and P. C. Loh, "Analysis and design of grid-current-feedback active damping for LCL resonance in grid-connected voltage source converters," *IEEE Trans. Power Electron.*, vol. 31, no. 1, pp. 213–223, Jan. 2016.

[25] V. Miskovic, V. Blasko, T. Jahns, A. Smith, and C. Romenesko, "Observer-based active damping of LCL resonance in grid-connected voltage source converters," *IEEE Trans. Ind. Appl.*, vol. 50, no. 6, pp. 3977–3985, Nov./Dec. 2014.

[26] J. Lei, B. Zhou, X. Qin, J. Wei, and J. Bian, "Active damping control strategy of matrix converter via modifying input reference currents," *IEEE Trans. Power Electron.*, vol. 30, no. 9, pp. 5260–5271, Sep. 2015.

[27] M. B. Said-Romdhane, M. W. Naouar, I. Slama-Belkhodja, and E. Monmasson, "Robust active damping methods for LCL filter-based grid-connected converters," *IEEE Trans. Power Electron.*, vol. 32, no. 9, pp. 6739–6750, Sep. 2017.

[28] W. Yao, X. Wang, P. C. Loh, X. Zhang, and F. Blaabjerg, "Improved power decoupling scheme for a single-phase grid-connected differential inverter with realistic mismatch in storage capacitances," *IEEE Trans. Power Electron.*, vol. 32, no. 1, pp. 186–199, Jan. 2017.


**Songwei Huang** was born in Fujian Province, China. He received the B.S. degree, from the School of Electrical Engineering, Beijing Jiaotong University, Beijing, China, in 2016, where he is currently working toward the M.S. degree.

His current research includes control strategy of power converters for renewable energy system.

**Fen Tang** received the B.S. degree in electrical engineering and the Ph.D. degree in power electronics and electric drives from Beijing Jiaotong University, Beijing, China, in 2006 and 2013, respectively.

She was a Guest Postdoctoral Researcher with the Department of Energy Technology, Aalborg University, Aalborg, Denmark, from 2013 to 2014. Since 2015, she has been a Lecturer with Beijing Jiaotong University. Her research interests include microgrids, wind power generation systems, power converters for renewable generation systems, power quality, and motor control.

**Zhen Xin** was born in Shandong Province, China. He received the B.S. and M.S. degrees from China University of Petroleum, Beijing, China, in 2011 and 2014, respectively, and the Ph.D. degree from Aalborg University, Aalborg, Denmark, in 2017, all in electrical engineering.

In 2016, he was a Visiting Scholar with the University of Padova, Padua, Italy. Since June 2017, he has been with the Chinese University of Hong Kong, Hong Kong, as a Postdoctoral Research Fellow. His research interests include power quality, modeling and control of power converters for renewable energy systems, gate-driver design for WBG devices, and Rogowski current sensor.

**Qi Xiao** was born in Chongqing Municipality, China, in 1993. He received the B.S. degree, in 2016, from the School of Electrical Engineering, Beijing Jiaotong University, Beijing, China, where he is currently working toward the M.S. degree.

His research interests include modeling and control analysis of power converters in renewable energy system.

**Poh Chiang Loh** received his B.Eng. (Hons.) and M.Eng. degrees from the National University of Singapore, Singapore, Singapore, in 1998 and 2000, respectively, and the Ph.D. degree from Monash University, Melbourne, VIC, Australia, in 2002, all in electrical engineering.

His interests include power converters and their grid applications.